

A modeling study of estuarine–shelf circulation using a composite tidal and subtidal open boundary condition

Zhiqiang Liu^{a,b}, Jianping Gan^{b,*}

^a Department of Ocean Science and Engineering, Southern University of Science and Technology, Shen Zhen, China

^b Department of Ocean Science and Department of Mathematics, The Hong Kong University of Science and Technology, Hong Kong, China

ABSTRACT

We investigated the performance of a tidally and subtidally forced open boundary condition (TST-OBC) on the estuarine–shelf circulation in a limited-area, down-scaling numerical modeling system for the northern South China Sea. We forced the modeling system with amplified tidal forces and subtidal forcing of spatiotemporally variable wind and river discharge. TST-OBC numerically and physically accommodates the circulation driven by the regional tides, subtidal forces, external forcing from its upscale solution, and internally generated disturbances. The advantages of TST-OBC are the separation of fast tidal and slow subtidal modes, active and dual-wave transmitting schemes, consistent treatment of barotropic and baroclinic circulation, and thermodynamic variables, which enable the model to capture observed circulation characteristics. The results differ from the results obtained using the Flather-type OBC, which over-restores internal to external solutions with a notable accumulation of spurious disturbances along the open boundaries. Disturbances with both tidal and subtidal signals that arrive at the open boundaries are well-treated by adopting TST-OBC, although it is currently feasible for the one-way downscaling applications.

1. Introduction

In numerical simulations of ocean circulation in a size-limited area, the open boundary condition (OBC) crucially impacts the interior solutions. However, implementing the OBC is an “ill-posed” problem (Oliger and Sundström, 1978). The reduced physics and simplified mathematics have led to improperly imposed “external” forces and reflective evacuation of “internal” disturbances at the open boundaries. A wrongly adapted OBC prevents a sensible connection between the internal and external forces and distorts the interior solution. This distorted solution is greater in shelf simulations where strong tidal and subtidal forces drive the hydrodynamically complex circulation (Bourret et al., 2005).

Sommerfeld (1949) originally proposed the radiation condition and Orlandi (1976), further generalized this condition. The radiation condition is the foundation of the most widely used conditions in modern ocean models. This Orlandi-type condition parameterizes propagating information across the open boundaries as nondispersive and unforced shallow water waves. Its equation is:

$$\phi_t + C\phi_N = 0, \quad (1)$$

where C is the propagation speed of the dependent variable, ϕ , and the subscripts, t and N , represent partial differentiation in time and horizontal space (usually in the cross-boundary direction), respectively.

The Orlandi-type condition inspired numerous different schemes, as summarized by Chapman (1985), Tsynkov (1998), Palma and Matano (1998, 2000), and Marsaleix et al. (2006). These schemes, in

most cases, are used to solve circulation without tidal forcing, and their dynamics are defined by how C in Eq. (1) is determined, and how the disturbances arriving at the open boundaries are treated (Blayo and Debret, 2005).

Properly including the exterior solution with a sensible scheme for C , with respect to the characteristics of the arriving disturbances, facilitates a less-reflective connection between the interior and exterior circulation, and forms “active” radiation OBCs (Gan and Allen, 2005; Gan et al., 2005). Schemes that exclude the exterior solution (forcing) are “passive” radiation OBCs (Blayo and Debret, 2005). Gan and Allen (2005) suggested subtracting the exterior solution from the model’s variables, and solving for the “global” solution by using the Orlandi-type radiation in Eq. (1). The radiation OBC was valid only for unforced flow, in principle, and effective for slow subtidally forced currents at the open boundary. The radiation OBC cannot solve for the circulation in an estuary or coastal waters where tidal forcing is amplified and where tidal and subtidal currents exist simultaneously.

Reid and Bodine (1968) presented that a wave propagating across a boundary can be sensibly simulated by specifying $C = \sqrt{gh}$ in the two-dimensional, depth-averaged momentum equation. g is the gravitational acceleration, and h is the water depth over the open boundary. Flather (1976) advanced Reid and Bodine’s approach by including the tidal current. Oey and Chen (1992) further included the subtidal elevation and current to form the widely-used “active” Flather-type boundary condition (FLA-OBC) for a barotropic current flowing perpendicular to an open boundary.

* Corresponding author.

E-mail address: magan@ust.hk (J. Gan).

While FLA-OBC effectively transmits tidal waves across the open boundary in a less reflective manner (Carter and Merrifield, 2007), the adaptability of the FLA-OBC in simulating the subtidal currents (for example, wind and buoyancy discharges) is questionable (Oddo and Pinardi, 2008) because of the dynamics on which FLA-OBC is based. The elevation and barotropic velocities are over-specified by FLA-OBC, and spurious kinetic energy accumulates at the open boundaries to create “rim currents” that prevent a sensible connection between the interior and exterior solutions in the computational domain (Mason et al., 2010). In addition, FLA-OBC has limited “noise” tolerance in the exterior solution and distorts the solutions in the baroclinic mode (Liu and Gan, 2016).

The inability of the Orlanski-type and Flather-type OBCs to sensibly resolve tidally and subtidally forced circulation across open boundaries in a limited-area simulation motivated the development of “active” schemes that overcame the drawbacks of FLA-OBC and the Orlanski-type OBC. Mason et al. (2010) proposed an improved FLA-OBC that separates the circulation at the open boundaries into components generated by internally and externally sourced surface gravity waves. They solve the internally sourced surface gravity waves by using “passive” schemes and the externally sourced ones by using “active” schemes with a specified $C = \sqrt{gh}$. In this paper, the Mason et al. (2010) scheme is called MAS-OBC.

The tidally and subtidally forced open boundary condition (TST-OBC), developed by Liu and Gan (2016), resolves tidal and subtidal wave propagation across the open boundaries in a different way that is more physically sensible. This research resolves tidal and subtidal signals by recognizing concurrently propagating tidal waves and subtidally generated disturbances and adapting the numerical and physical advantages of the OBCs of Oey and Chen (1992) and Gan and Allen (2005), respectively. The separate treatment of tidally and subtidally forced currents allows TST-OBC to be an “active and dual-wave transmitting” scheme, in which both tidal and subtidal (“dual-wave transmitting”) disturbances are sensibly transmitted through the open boundary, while the exterior solution from the upscale simulation is imposed. However, in Liu and Gan’s study, the TST-OBC was based on steady, constant, and spatially uniform wind and tidal forcing. The reliability of TST-OBC in solving the tidal current and subtidal circulation driven by regional and remote forcing with extensive spatiotemporal variability was not investigated.

In our current study, a multi-domain downscaling simulation system that focuses on the circulation in the Pearl River Estuary and adjacent shelf waters (L2 domain in Fig. 1) is developed to investigate the adaptability and accuracy of TST-OBC. Both field observations and circulation dynamics are used to validate the simulation system.

The study area is in the northern South China Sea (L1 domain in Fig. 1a), which has a complicated coastline and bathymetry that stretches northeastward along the coast of Guangdong Province, China. The water depth in the L2 domain (Fig. 1b) is generally shallower than 70 m, and the depth decreases shoreward. The interior circulation and hydrodynamics in our domain are regulated by energetic spatially and temporally variable tidal (Zu et al., 2008) and subtidal (wind and river discharge) forces (Gan et al., 2009a,b) and external forces from the large-scale slope and basin circulation of the connected L1 simulation (Gan et al., 2016). These jointly imposed forces produce complicated circulation patterns in the area (Zu and Gan, 2015).

Implementing the OBC so that the processes in the limited-area domain could communicate with the processes in the larger scale domain is critical and challenging in this multi-domain downscaling simulation system. In this study, the numerical and physical responses of TST-OBC to the spatiotemporally variable forcing of energetic and multi-constituent tidal forcing, strong shelf currents, winds, and buoyancy from river discharge are investigated. It is shown that TST-OBC has advantages in simulating shelf and estuarine circulation, when the circulation is jointly driven by spatiotemporal variable wind, buoyancy forcing, and tides.

2. Ocean model and TST-OBC

2.1. Ocean model

The Regional Ocean Modeling System (ROMS; Shchepetkin and McWilliams, 2005; Rutgers branch, <http://www.myroms.org>) is used for the downscaling simulations. ROMS solves the three-dimensional primitive equations in an Arakawa C-grid system. In ROMS, barotropic and baroclinic mode splitting effectively computes the external and internal motions. The level-2.5 turbulent kinetic energy equations from Mellor and Yamada (1982) parameterize the vertical mixing of the sub-model, and a third-order upwind-biased scheme solves for horizontal momentum advection. The multidimensional positive definite advection algorithm solves for the advection of temperature and salinity.

Three levels of models make up our downscaling system (Fig. 1a). The horizontal resolution gradually increases from the open ocean to the coastal seas. The interactions between the basin circulation in the South China Sea and large-scale circulation in the Northwest Pacific Ocean cascade from a hindcast simulation in the China Seas Multi-Scale Modeling System (L0 domain in Fig. 1; 10 km) [<https://odmp.ust.hk/cmoms/>, Gan et al., 2016] to the L1 domain (3 km) (Gan et al., 2015). The daily-averaged model results from the L1 simulation are used as exterior solutions for a high-resolution simulation over the shelf in the L2 domain (Fig. 1b). The L2 domain has been horizontally discretized into a matrix with 400×441 points using an orthogonal curvilinear grid system. The ultrahigh resolution (~ 0.1 km) resolves the estuary and the inner shelf that neighbors Hong Kong. The grid size gradually increases to ~ 1 km over the shelf at its southern boundary to smoothly connect with the circulation in the L1 domain. In this study, the circulation over the shelf of the L2 domain where the tidal and subtidal forces are amplified is examined. The L1 and L2 models have 30 vertical levels on terrain-following s -coordinates (Song and Haidvogel, 1994). There are higher resolutions (< 0.2 m) in the surface and bottom boundary layers. The L2 domain has three open boundaries (western, eastern, and southern) connecting to the L1 domain (Fig. 1b).

The L0, L1 and L2 simulations have been run from 2011 to 2015. To impose tidal forcing, M_2 , S_2 , K_2 , N_2 , K_1 , O_1 , Q_1 , P_1 , and M_4 tidal constituents at the open boundaries are extracted from the Oregon State University Tidal Inversion Software (OTIS) (Egbert and Erofeeva, 2002), which Zu et al. (2008) previously validated. Atmospheric forces from the European Center for Medium-Range Weather Forecasts (ECMWF) global reanalysis data are imposed by using the bulk formulation in Fairall et al. (2003). The atmospheric forcing interval is 3 h, and the horizontal resolution of the forcing fields is 0.175° . The Pearl River discharge rate from the upstream hydrographic monitoring station at Gaoyao is used in a daily forcing interval.

In this study, we took advantage of having available *in-situ* observations to validate our results. Field measurements over the northern Southern China Sea shelf during the summer of 2015 from July 1 to August 15 are conducted. The observations include time series observations and ship-based mapping at the stations shown in Fig. 1b. At the mooring station, a downward looking Acoustic Doppler Current Profiler (ADCP, 600 kHz) on a surface buoy is deployed for about 1.5 months of velocity data. Temperature and salinity in the water column at the ship-based mapping stations are measured with a conductivity–temperature–depth (CTD) profiler. Measured water levels from the tide gauge at Waglan Island, southeast of Hong Kong (Fig. 1b) are used to evaluate the performance of TST-OBC in resolving propagating tidal waves and subtidal variability of sea surface elevation.

NASA’s Jet Propulsion Laboratory provided remotely sensed sea surface temperature (SST) from the daily, global, multi-scale, ultrahigh resolution SST dataset at 1 km resolution. This SST observation is used to investigate the response of the shelf current to the jointly imposed tidal and subtidal forces at the sea surface.

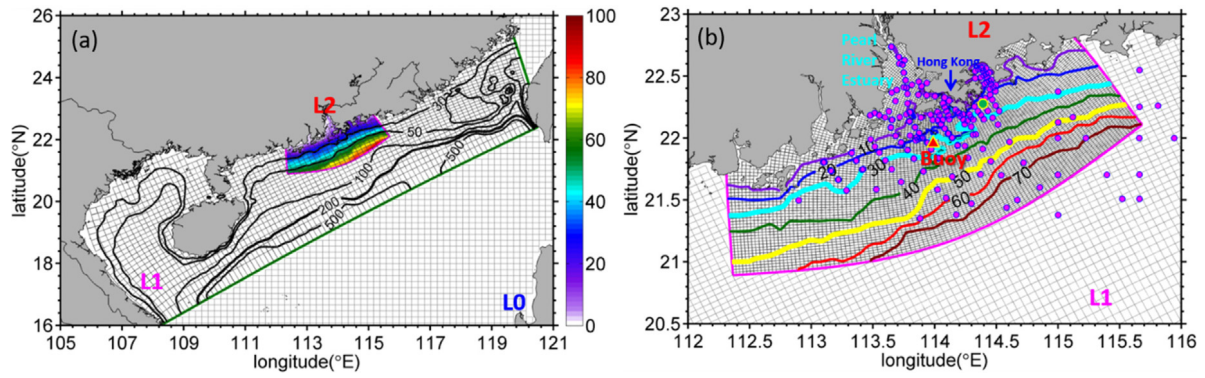


Fig. 1. (a) The computational grid of the L0 model from the China Sea Multi-Scale Ocean Modeling System in the South China Sea and in the northern South China Sea (L1 model); and (b) computational grid of the L1 and L2 simulations neighboring the Pearl River Estuary. The 30 m, 50 m, 100 m, 200 m, and 500 m isobaths, and the bathymetry (m) in the L2 domain for shelf circulation in the coastal area neighboring Hong Kong are shown in (a). The 10 m to 70 m isobaths in the L2 simulation are shown in (b). The pink dots in (b) are the locations of the field stations, and the green dot shows the position of the tide gauge at Waglan Island. The red triangle shows the location of the moored buoy where the water velocity is monitored with a downward-looking ADCP.

2.2. TST-OCB

The model subdomains are linked by TST-OCB, which, as detailed in Liu and Gan (2016), separates the subtidal and tidal components of the cross-boundary depth-averaged velocity (\bar{u}). TST-OCB also uses “active” schemes in the barotropic mode to solve for the components. In this research, the notations, R and T , represent the subtidal and tidal components of the barotropic velocities (\bar{u}) normal to the open boundaries and are respectively expressed as \bar{u}_{Rb}^{n+1} and \bar{u}_{Tb}^{n+1} . The notations in this section and relationships among the equations in this section are summarized in Table 1, and the operation flowchart of TST-OCB is in Table 2.

The formula for TST-OCB is:

$$\bar{u}_b^{n+1} = \begin{cases} \left[\bar{u}_{Rb}^n - \frac{\Delta t}{\lambda} (\bar{u}_{Rb}^n - \bar{u}_{Rlb}^n) \right] + \bar{u}_{Tlb}^{n+1} \\ \pm \sqrt{\frac{g}{H}} (\eta_b^{n+1} - \eta_{Tlb}^{n+1} - \eta_{Rlb}^{n+1}) & (C \leq 0) \\ \left[\bar{u}_{Rlb}^{n+1} + \frac{1}{1+C} (\bar{u}_{RGb}^n + C\bar{u}_{RG(b\pm 1)}^{n+1}) \right] + \bar{u}_{Tlb}^{n+1} \\ \pm \sqrt{\frac{g}{H}} (\eta_b^{n+1} - \eta_{Tlb}^{n+1} - \eta_{Rlb}^{n+1}) & (C > 0). \end{cases} \quad (2)$$

λ , which is one hour in this study, is the relaxation time for the inflow condition with the phase speed of the disturbances, $C \leq 0$.

In Eq. (2), G represents the “global” solution of TST-OCB. Therefore, the “global” solution for tidal currents (\bar{u}_{TGb}^{n+1}) is:

$$\bar{u}_{TGb}^{n+1} = \pm \sqrt{\frac{g}{H}} (\eta_b^{n+1} - \eta_{Tlb}^{n+1} - \eta_{Rlb}^{n+1}), \quad (3)$$

in which, ‘ \pm ’ in Eqs. (2) and (3) depends on the boundary. A negative sign (‘ $-$ ’) denotes solving for barotropic velocities at the southern and western open boundaries, and a positive sign (‘ $+$ ’) denotes solving for barotropic velocities at the northern and eastern open boundaries.

Switching TST-OCB for inward or outward propagating disturbances associated with subtidal current is determined by C , which is the phase speed calculated from the “global” solutions of the Orlandi-type (implicit) radiation condition (Marchesiello et al., 2001). Therefore, C is solved using:

$$C = \frac{\bar{u}_{RG(b\pm 1)}^n - \bar{u}_{RG(b\pm 1)}^{n+1}}{\bar{u}_{RG(b\pm 1)}^{n+1} - \bar{u}_{RG(b\pm 2)}^{n+1}}. \quad (4)$$

This expression shows that C depends on the barotropic velocities at two grids that are next to the open boundaries inside the computational domain.

To further elaborate the physical meaning of Eq. (2), and make the expression clearer, the first term on the right-hand side is defined as:

$$\bar{u}_{Rb}^{n+1} = \begin{cases} \bar{u}_{Rb}^n - \frac{\Delta t}{\lambda} (\bar{u}_{Rb}^n - \bar{u}_{Rlb}^n) & (C \leq 0) \\ \bar{u}_{Rlb}^{n+1} + \frac{1}{1+C} (\bar{u}_{RGb}^n + C\bar{u}_{RG(b\pm 1)}^{n+1}) & (C > 0), \end{cases} \quad (5)$$

in which, as stated previously, \bar{u}_{Rlb}^{n+1} stands for the daily- and depth-averaged velocity from the upscaled simulation.

Eq. (2) is then shortened and further clarified into:

$$\bar{u}_b^{n+1} = \bar{u}_{Rb}^{n+1} + \bar{u}_{Tlb}^{n+1} + \bar{u}_{TGb}^{n+1}. \quad (6)$$

To evaluate the function of the “active” radiation condition for the residual current in Section 4.3, the “global” solution for subtidal current (\bar{u}_{RGb}^{n+1}) is computed with:

$$\bar{u}_{RGb}^{n+1} = \bar{u}_{Rb}^{n+1} - \bar{u}_{Rlb}^{n+1}. \quad (7)$$

Eq. (7) is not explicitly used in the TST-OCB scheme.

Using FLA-OCB reveals the characteristics of TST-OCB. The formula for FLA-OCB is:

$$\bar{u}_b^{n+1} = \bar{u}_{Rlb}^{n+1} + \bar{u}_{Tlb}^{n+1} + \bar{u}_{TGb}^{n+1}. \quad (8)$$

Eqs. (6) and (8), as well as Table 1, clearly show that the major difference between TST-OCB and FLA-OCB is the solution for the subtidal current (\bar{u}_{Rb}^{n+1}). For TST-OCB, an “active” scheme in Eq. (5) taken from Roed and Smedstad (1984) is used. The “active” scheme evacuates the non-tidal disturbances (\bar{u}_{RGb}^{n+1}) in Eq. (7), and the exterior solutions (\bar{u}_{Rlb}^{n+1}) preserve the dynamic similarity between the interior and exterior solutions because the latter solution is retrieved from solving the primitive equations without having to dynamically simplify much in the L1 domain. The low (subtidal) and high (tidal) frequency disturbances are, therefore, solved in an “active” manner with a “dual-wave transmitting” scheme. In contrast, FLA-OCB specifies the exterior solutions at the open boundaries by using $\bar{u}_{Rb}^{n+1} = \bar{u}_{Rlb}^{n+1}$. The term, \bar{u}_{TGb}^{n+1} , in Eq. (8) only allows barotropic tidal waves to radiate across the open boundaries, so using FLA-OCB results in an “active” but “single-wave transmitting” scheme.

TST-OCB can be applied to the three-dimensional momentum equations by excluding the solution for barotropic tidal waves. This treatment preserves the dynamic consistency between barotropic and baroclinic motions across the open boundaries, as shown in Table 1. To preserve that consistency through omitting the last term in the right-hand-side of Eq. (2), or:

$$\bar{u}_b^{n+1} = \begin{cases} \left[\bar{u}_{Rb}^n - \frac{\Delta t}{\lambda} (\bar{u}_{Rb}^n - \bar{u}_{Rlb}^n) \right] + \bar{u}_{Tlb}^{n+1} & (C \leq 0) \\ \left[\bar{u}_{Rlb}^{n+1} + \frac{1}{1+C} (\bar{u}_{RGb}^n + C\bar{u}_{RG(b\pm 1)}^{n+1}) \right] + \bar{u}_{Tlb}^{n+1} & (C > 0). \end{cases} \quad (9)$$

Table 1
Links among the equations discussed in Section 2.2.

	TST-OBC (E_{TST})	FLA-OBC (E_{FLA})
barotropic solution	<p>sub-tidal exterior solution from upscale (L1) simulation</p> <p>Equation (2)</p> $\bar{u}_b^{n+1} = \begin{cases} \left[\bar{u}_{Rb}^n - \frac{\Delta t}{\lambda} (\bar{u}_{Rb}^n - \bar{u}_{Rlb}^n) \right] + \bar{u}_{Tlb}^{n+1} \pm \sqrt{\frac{g}{H}} (\eta_b^{n+1} - \eta_{Tlb}^{n+1} - \eta_{Rlb}^{n+1}) & (C \leq 0) \\ \left[\bar{u}_{Rlb}^{n+1} + \frac{1}{1+C} (\bar{u}_{Rcb}^n + C \bar{u}_{RG(b\pm 1)}^{n+1}) \right] + \bar{u}_{Tlb}^{n+1} \pm \sqrt{\frac{g}{H}} (\eta_b^{n+1} - \eta_{Tlb}^{n+1} - \eta_{Rlb}^{n+1}) & (C > 0) \end{cases}$	
	<p>Equation (6)</p> $\bar{u}_b^{n+1} = \bar{u}_{Rb}^{n+1} + \bar{u}_{Tlb}^{n+1} + \bar{u}_{TGb}^{n+1}$ <p>$C = \frac{\bar{u}_{RG(b\pm 1)}^n - \bar{u}_{RG(b\pm 1)}^{n+1}}{\bar{u}_{RG(b\pm 1)}^{n+1} - \bar{u}_{RG(b\pm 2)}^{n+1}}$</p>	<p>Equation (8)</p> $\bar{u}_b^{n+1} = \bar{u}_{Rlb}^{n+1} + \bar{u}_{Tlb}^{n+1} + \bar{u}_{TGb}^{n+1}$
baroclinic solution	<p>Equation (9)</p> $u_b^{n+1} = \begin{cases} \left[u_{Rb}^n - \frac{\Delta t}{\lambda} (u_{Rb}^n - u_{Rlb}^n) \right] + \bar{u}_{Tlb}^{n+1} & (C \leq 0) \\ \left[u_{Rlb}^{n+1} + \frac{1}{1+C} (u_{Rcb}^n + C u_{RG(b\pm 1)}^{n+1}) \right] + \bar{u}_{Tlb}^{n+1} & (C > 0) \end{cases}$ <p>$C = \frac{u_{RG(b\pm 1)}^n - u_{RG(b\pm 1)}^{n+1}}{u_{RG(b\pm 1)}^{n+1} - u_{RG(b\pm 2)}^{n+1}}$</p>	

Δt is the timestep of the external mode in ROMS. l represents exterior solutions. g is the gravitational acceleration. H is the total water depth. η is surface elevation.

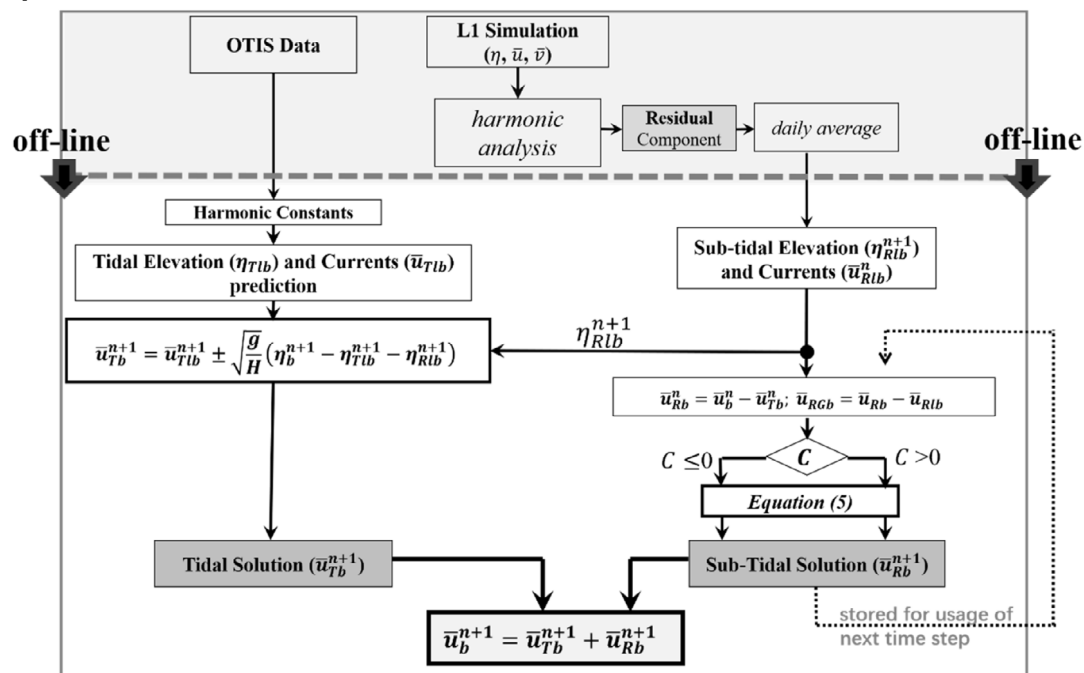
n represents the current time level and $n + 1$ stands for one timestep forward from the current time level or the timestep when solutions at open boundaries are requested.

b stands for the grid points at the open boundaries. $b \pm 1$ and $b \pm 2$ here and in equation (2) represent these two grids, respectively. A positive sign ('+') stands for solutions neighboring the southern and western open boundaries, and a negative sign ('-') stands for solutions neighboring the northern and eastern open boundaries.

$(\eta_{Tlb}^{n+1}, \bar{u}_{Tlb}^{n+1})$ are tidal elevation and depth-averaged tidal velocity normal to the open boundaries from tidal prediction based on harmonic constants extracted from the OTIS dataset.

$(\eta_{Rlb}^{n+1}, \bar{u}_{Rlb}^n, \bar{u}_{Rlb}^{n+1})$ are detided and daily-averaged surface elevation and depth-averaged velocity from the upscale simulation, respectively. They act as exterior solution of this scheme.

Table 2
Operation flowchart of the TST-OBC revised from Liu and Gan (2016).



Note that the depth-averaged velocity (\bar{u}) in Eq. (2) was replaced with the depth-dependent velocity (u), except in the predicted tidal velocity

(\bar{u}_{Tlb}^{n+1}) . Based on Eq. (3), C is computed by using u . For dynamic consistency in the problem, an “active” scheme is used to solve for

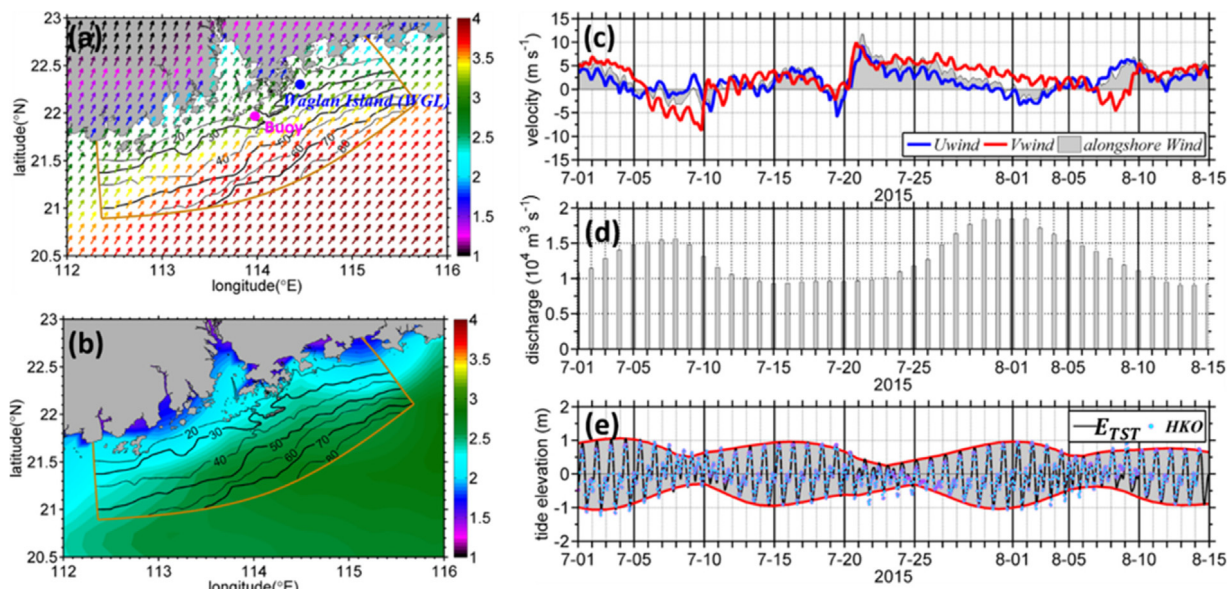


Fig. 2. (a) Horizontal maps of time-averaged wind velocity (m s^{-1}) vectors in the L1 domain and (b) standard deviation of the wind velocity magnitude (m s^{-1}) from July 1 to August 15, 2015; (c) time series of horizontally averaged wind velocity in zonal (blue) and meridional (red) directions and time series of the horizontally averaged along-shore component of the wind velocity in the L2 domain (gray area); (d) time series of river discharge from the Pearl River; and (e) simulated time series of water level at the tide gauge from E_{TST} (black line) and observed water level time series (dots). The red curves and gray area in (e) denote the variation of daily maximum/minimum water level from July 1 to August 15, 2015.

Table 3
Summary of the OBC configuration in sensitivity experiments.

	OBC configuration		
	Barotropic velocity (\bar{u})	Barotropic velocity (u)	Temperature and salinity
P_{TST}	TST-OBC	TST-OBC	TST-OBC
E_{TST}	TST-OBC	TST-OBC	TST-OBC
E_{FLA}	FLA-OBC	TST-OBC	TST-OBC
E_{MAS}	MAS-OBC	TST-OBC	TST-OBC
E_{ROMS}	FLA-OBC	Marchesiello et al. [2001]	Marchesiello et al. [2001]

the temperature and salinity at the open boundaries as in Liu and Gan (2016). λ is set as 12 hours for the baroclinic velocities normal to the boundaries, temperature, and salinity in this study.

The advantages of using TST-OBC are summarized as being able to:

(a) decompose the subtidal and tidal dynamics and separate the exterior solution and “global” components of the subtidal flows normal to the boundaries according to their respective physical and numerical natures,

(b) apply active and dual-wave transmitting schemes for tidal and subtidal currents,

(c) tolerate the discrepancy between solutions from the L2 and L1 domains through the “global” solution (Eq. (7)),

(d) provide consistent adaptation among all barotropic and baroclinic variables in the OBC to ensure dynamic consistency.

In the following sections of this paper, the simulations using TST-OBC in the L1 and L2 domains are named, P_{TST} and E_{TST} , respectively. The OBC configurations for barotropic, baroclinic velocities, temperature and salinity in different experiments are summarized in Table 3.

3. The tidally and subtidally forced shelf circulation

3.1. The forcing conditions

Fig. 2a and b show the horizontal distribution of wind vectors at 10 m above the sea surface and the standard deviation of the wind magnitude (95% confidence interval). The wind field in Fig. 2a is the

average over the field cruise period (July 1 to August 15, 2015). Fig. 2c illustrates the time series of zonal and meridional wind speed and the time series of its alongshore component averaged over the L2 domain. A positive alongshore wind blew northeastward ($\sim 22.8^\circ$ to the east). The time series of the Pearl River discharge rate is in Fig. 2d, and e shows the time series of the simulated and observed surface elevations at the tide gauge on Waglan Island.

Fig. 2a and b clearly show that the southwesterly summer monsoon prevailed during the field cruise. The wind intensity was stronger offshore towards the central South China Sea basin where its standard deviation was comparable to the wind magnitude. Both zonal and meridional winds demonstrated extensive variations in synoptic time-scales, manifested by abrupt wind speed changes from July 19 to July 21, when a short-term and weak downwelling-favorable northeasterly wind rapidly reversed to become upwelling-favorable within a single day (July 20).

The strong buoyancy discharge from the Pearl River influenced the subtidal circulation in the study area (Fig. 2d) (Zu et al., 2014), and the average discharge rate at Gaoyao station was $\sim 1.2 \times 10^4 \text{ m}^3 \text{ s}^{-1}$, consistent with typical summer conditions. High frequency tidal forcing strongly influenced the estuarine–shelf circulation in the study area (Fig. 2e). The dominant constituents were M_2 and K_1 (Zu et al., 2008), and the tide amplified as it entered the shallower L2 domain.

3.2. Tidal dynamics

The reliability of TST-OBC in solving high frequency tidal currents is at first examined. Fig. 2e shows the agreement between the simulated tidal elevation at Waglan Island and the observed water levels. The estimated correlation coefficient between the observed and simulated tidal elevation is ~ 0.96 (with 95% confidence interval). The coefficient of determination (R^2) is greater than 0.83, and the root mean square error is smaller than 0.05 m. Harmonic analysis (Pawlowicz et al., 2002) of the simulated surface elevation from E_{TST} allows us to extract the horizontal maps of amplitude and phase-lag of the tidal elevation for M_2 and K_1 (Fig. 3). The simulated harmonic constants are compared with the constants obtained from the OTIS dataset. Horizontal maps of the tidal amplitudes for M_2 and K_1 from the C_{TST} simulation and the OTIS observations clearly illustrate that the tides intensified shoreward

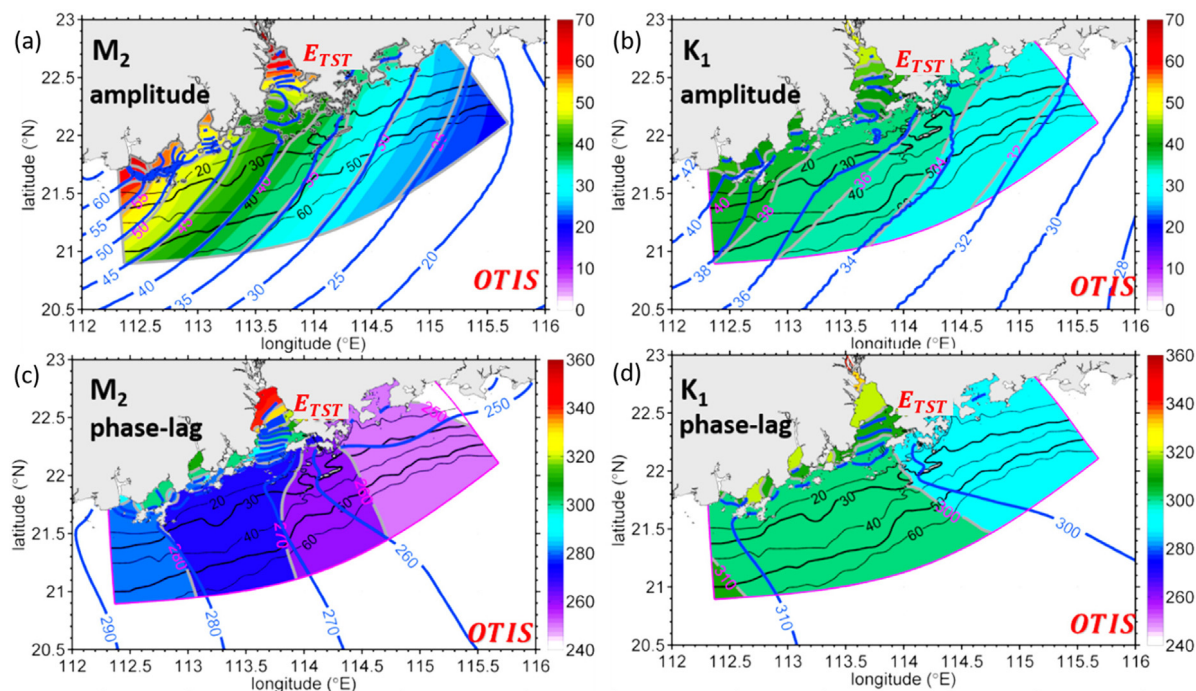


Fig. 3. Cotidal charts of (a, b) tidal amplitude (cm) and (c, d) phase-lag (degrees) for (a, c) M_2 and (b, d) K_1 constituents from the E_{TST} simulation (colored area) and OTIS observations (blue contours), respectively.

and westward in the L2 domain (Fig. 3). The maximum tidal amplitude over the inshore area of the western boundary exceeds 0.4 m. The horizontal maps of phase-lag further show that tidal waves propagate cyclonically over the shelf, with K_1 traveling faster than M_2 .

Now, the observed and simulated tidal velocities at the ADCP buoy location are examined. The time series of the observed depth-averaged meridional and zonal velocities at the buoy agrees well with the simulated ones. The correlation coefficients between the simulated and long-term recorded tidal velocities in both directions exceed 0.96 (with 95% confidence interval). The R^2 value is greater than 0.90, and the root mean square error is smaller than 0.04 m s^{-1} . These error-analyses show the agreement between observations and simulation from E_{TST} .

This agreement between observed and simulated tidal data demonstrates the reliability of TST-OBC in accommodating tidal forcing that is imposed along the open boundaries of a computational domain (Fig. 4). Consistent with Fig. 3c and d, the tidal current oscillated zonally. The amplitude of the tidal current was over $0.3/0.15 \text{ m s}^{-1}$ for the spring/neap tides. Fig. 4 also shows that, although tides imposed the strongest fluctuation in the currents, there was a notable subtidal current. The subtidal current generally flowed northeastward when an upwelling-favorable wind prevailed, and weakened or reversed direction when strong downwelling-favorable winds blew.

3.3. Subtidal shelf circulation

The response of the shelf current to the subtidal forces of wind and buoyancy discharge is shown in the simulated surface and bottom velocity vectors and salinity distributions (Fig. 5). Fig. 6a shows the satellite remote sensed SST averaged over the cruise period. Fig. 6b displays the observed bottom temperature distribution obtained from the deepest CTD measurement at each station. The simulated temperature distributions in the surface and bottom layers, averaged over the cruise period in the L2 domain, are shown in Fig. 6c and d, respectively. The T-S diagrams of the observed and E_{TST} simulated temperature and salinity at each station are shown in Fig. 7a, and the observed and simulated water temperatures are compared in Fig. 7b for all the stations.

To discuss the adaptability and reliability of TST-OBC further, a sensitivity experiment is configured in the L2 domain that kept the dynamic implementation and numerical configuration in E_{TST} , but switched to the recommended OBC configurations in ROMS. This case is named E_{ROMS} (Table 3). It should be noted that FLA-OBC is used to solve for barotropic velocity, and the adaptive radiation condition in Marchesiello et al. [2001] is used to solve for the baroclinic velocities, temperature, and salinity in E_{ROMS} . The T-S diagrams of the observed and simulated temperature and salinity and the comparison of the temperatures for all the stations from E_{ROMS} are shown in Fig. 7c and d.

In Fig. 5a, a pronounced northeastward shelf current appeared in response to the southwesterly wind forcing shown in Fig. 2a. This current occupied the water over the shelf and extended to the bottom layer where there were upslope velocities (Fig. 5b). The shelf current intensified from the western to the eastern boundary and was stronger over the shelf in the lee of Hong Kong (Fig. 5a). The extensive buoyancy plume due to riverine freshwater discharged from the Pearl River Estuary caused the shelf current to be spatially variable (Fig. 5c). Over the shelf, the current intensified on the shore-side of the density front due to the strengthened shoreward pressure gradient force, while it weakened on the seaside (Liu et al., 2018). This strengthening/weakening pattern is consistent with the result obtained by Gan et al. (2009b).

In response to the upwelling, deep shelf waters were advected upslope towards the coastal ocean which is seen in the simulated and observed temperature distributions (Fig. 6). This upslope transport prevented the buoyant plume from being bottom-advected over the shelf deeper than 20 m (Fig. 5d), and, in response to the eastward strengthened coastal current (Fig. 5a and b), the onshore invasion of deep shelf waters strengthened eastward in the L2 domain (Figs. 5d, 6b and d). These cold waters extended over the shelf in the surface layer in the lee of Hong Kong and formed a notable surface cold water belt (Fig. 6a and c).

The E_{TST} simulated surface salinity further revealed that the buoyant river plume expanded bi-directionally (both eastward and westward) and was enveloped by a sharp density front along its edge (Fig. 5c and d). The water inside the E_{TST} plume was fresher than the plume water from P_{TST} due to E_{TST} resolving the plume dynamics better. The notable fluctuation around the 40 m isobath shows that

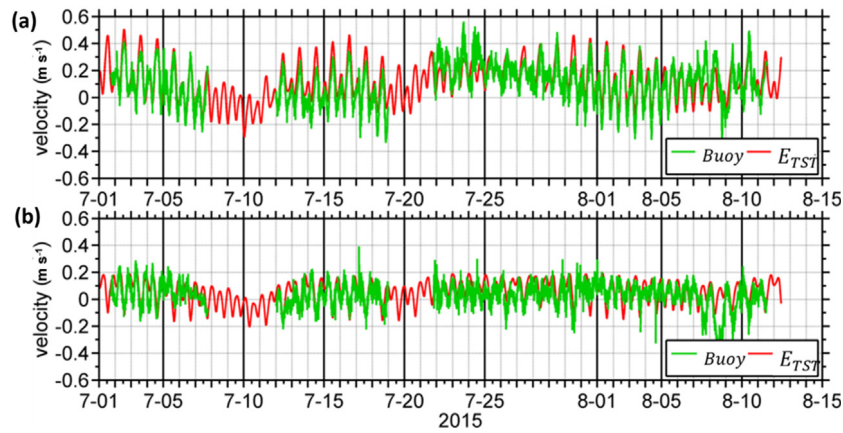


Fig. 4. Time series of depth-averaged (a) zonal and (b) meridional velocities (m s^{-1}) measured by the ADCP (Buoy) and from the E_{TST} simulation. The location of the ADCP moored buoy is shown in Fig. 1b.

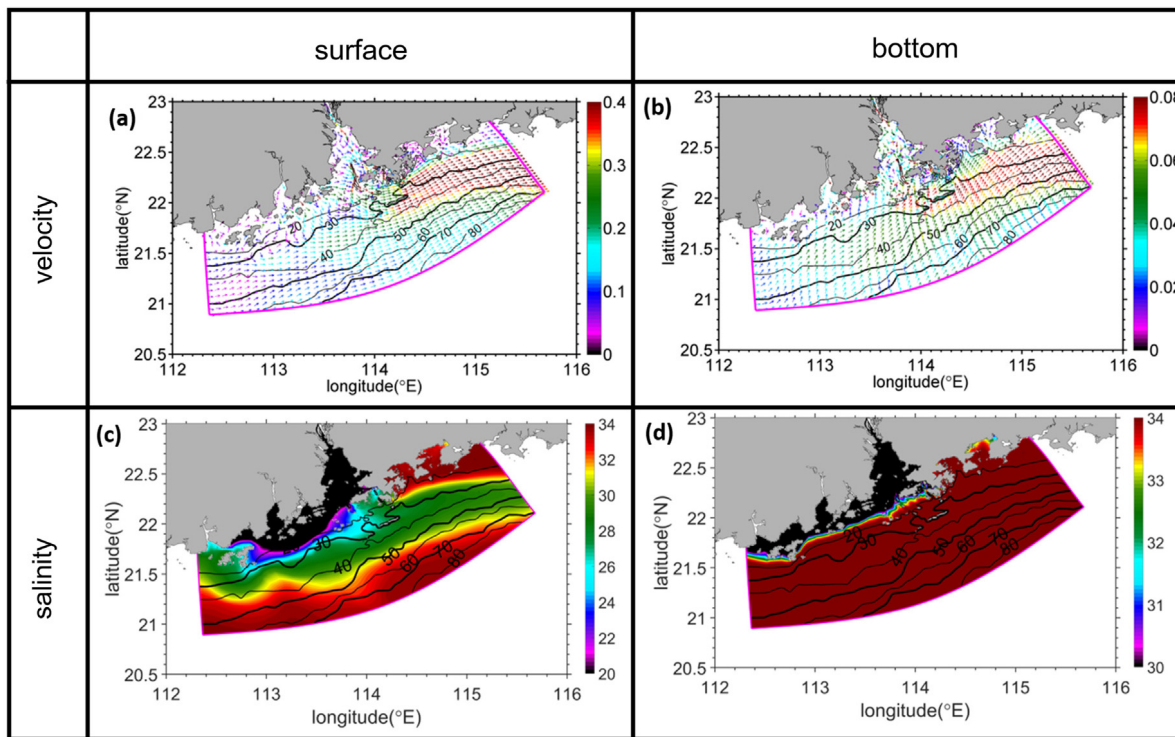


Fig. 5. Horizontal maps of (a, b) velocities (m s^{-1}) and (c, d) salinity (psu) in the (a, c) surface and (b, d) bottom layers of the E_{TST} simulation. The velocities and salinity fields from the E_{TST} simulation were averaged over the cruise period.

this fresher plume meandered extensively in the western half of the computational domain (Fig. 5c). The thickness of this buoyant plume was 10 m, and the westward branch of the buoyant water attached to the seabed over the inshore area (Fig. 5d).

It is now clear that, nested by TST-OBC, the downscaling system captured the general characteristics of the tidal current and subtidal circulation in the study area. The reliability of TST-OBC is elaborated with the time-series of the sea surface height (Fig. 2e) and velocities (Fig. 4), and by comparing the simulated and observed T-S diagrams and temperature fields (Fig. 7a and b). The correlation coefficient between the observed and simulated temperature in the water column is 0.93 (95% confidence interval), and the R^2 value is over 0.8 in E_{TST} . A root mean square error analysis shows that the discrepancy between the E_{TST} simulation and field measurements is smaller than 1.2 °C for temperature and 2.3 psu for salinity. However, when the recommended OBC configuration in ROMS is adopted for E_{ROMS} , the correlation

coefficient and R^2 values reduce to 0.53 and 0.0, respectively. Fig. 7 also clearly shows that, for the E_{ROMS} case, not using TST-OBC causes the physical properties of the shelf water to deviate more from the observations (Fig. 7c), and excessive mixing occurs in the lower layers where there is a much larger discrepancy (Fig. 7d).

4. Rationale of OBCs

In this section, the performance of TST-OBC's response to variable forcing (Fig. 2) for the cruise period is detailed. To rationalize the success of TST-OBC in simulating tidal and subtidal currents, two additional sensitivity experiments in the L2 domain are conducted by using FLA-OBC and MAS-OBC in the Rutgers ROMS to solve for the barotropic velocities (Table 3). Unlike E_{ROMS} , TST-OBC is used to solve for the baroclinic velocities, temperature, and salinity in these new experiments to avoid the disadvantages identified in our earlier

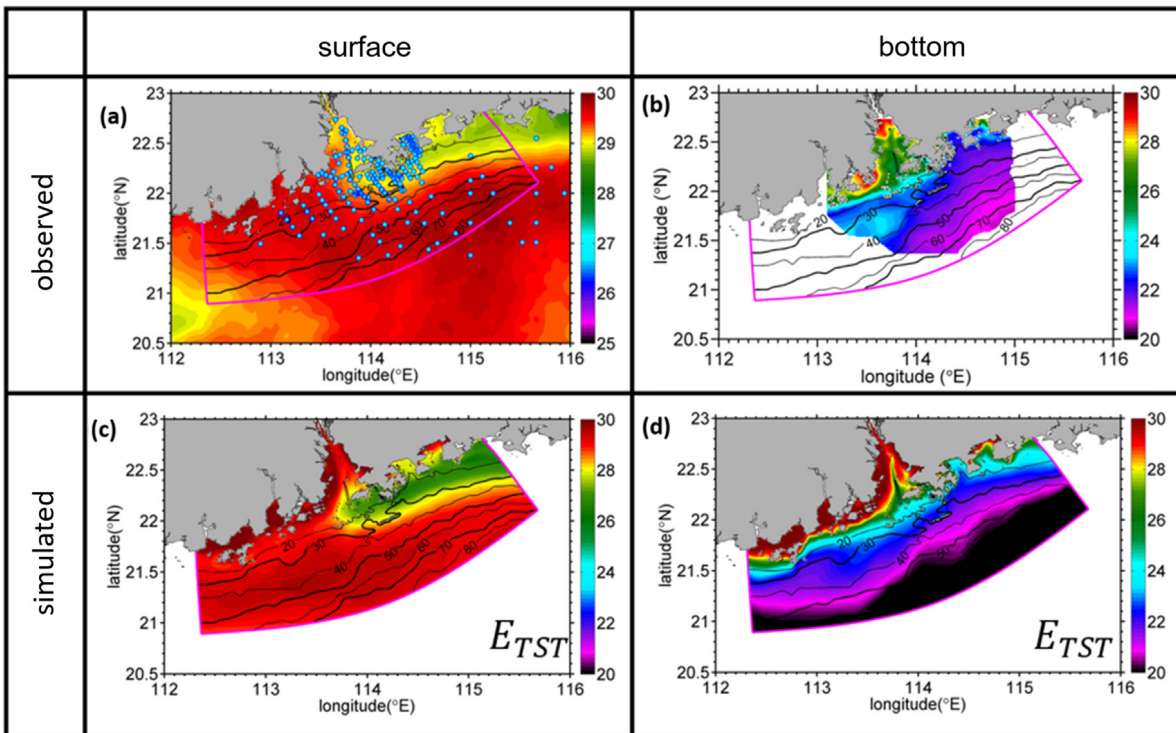


Fig. 6. Horizontal maps of (a) remotely sensed sea surface temperature ($^{\circ}\text{C}$) in the northern South China Sea, (b) distribution of measured temperature over the seabed, and simulated (c) sea surface and (d) bottom temperature in the surface and bottom layers in L2. The sea surface temperature in (a) and the temperature field from the E_{TST} simulation in (c) and (d) were averaged over the cruise period.

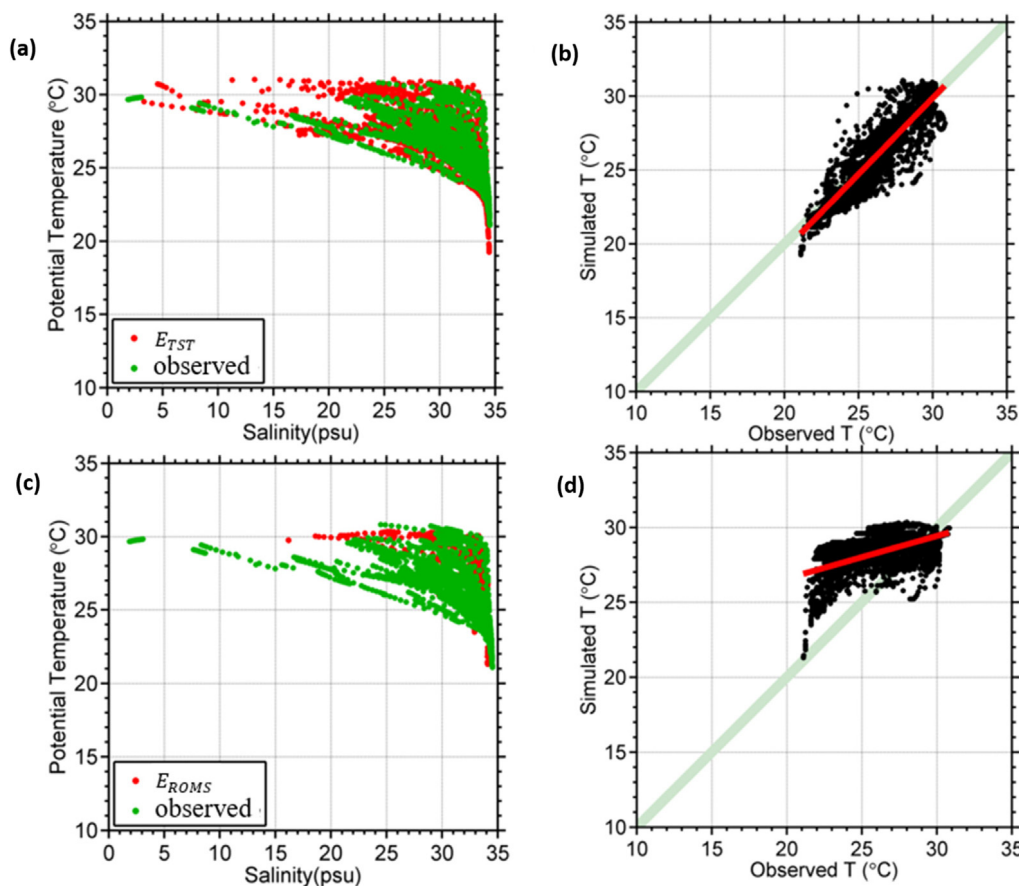


Fig. 7. (a, c) T-S diagrams and (b, d) temperature comparisons at all stations. The red line shows the linear regression between observations and simulations from (a, b) E_{TST} and (c, d) E_{ROMS} .

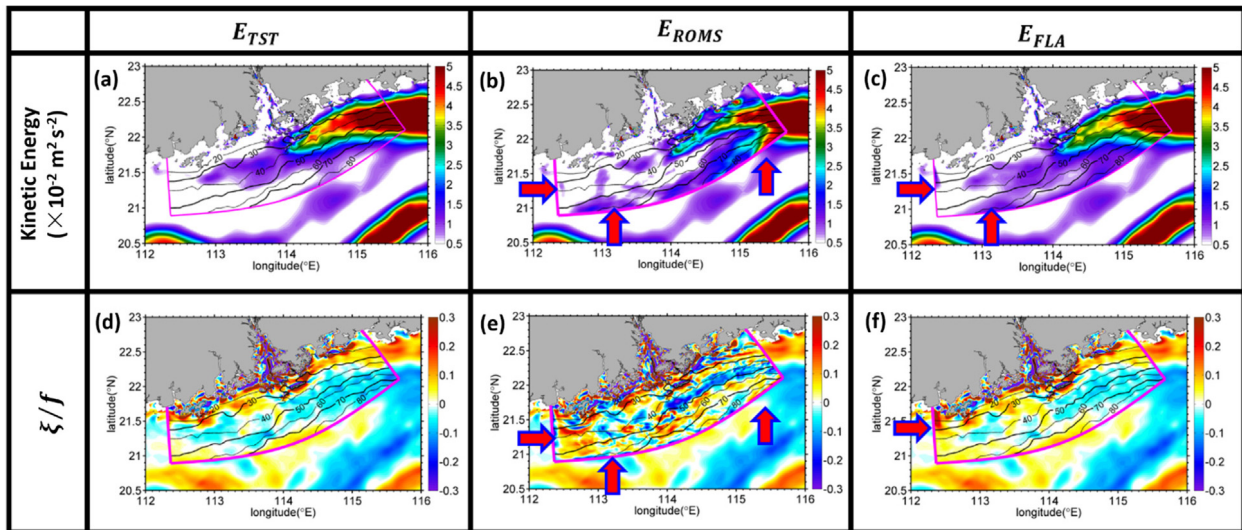


Fig. 8. Horizontal maps of simulated depth-averaged (a–c) kinetic energy ($10^{-2} \text{ m}^2 \text{ s}^{-2}$) and (d–f) R_o from (a, d) E_{TST} , (b, e) E_{ROMS} , and (c, f) E_{FLA} . Results from P_{TST} , outside the L2 domain (pink line), are presented in the same map. The simulated velocities were averaged over the cruise period, and the red arrows in (b, c) and (e, f) highlight the location where the discrepancy between L1 and L2 simulations is discussed.

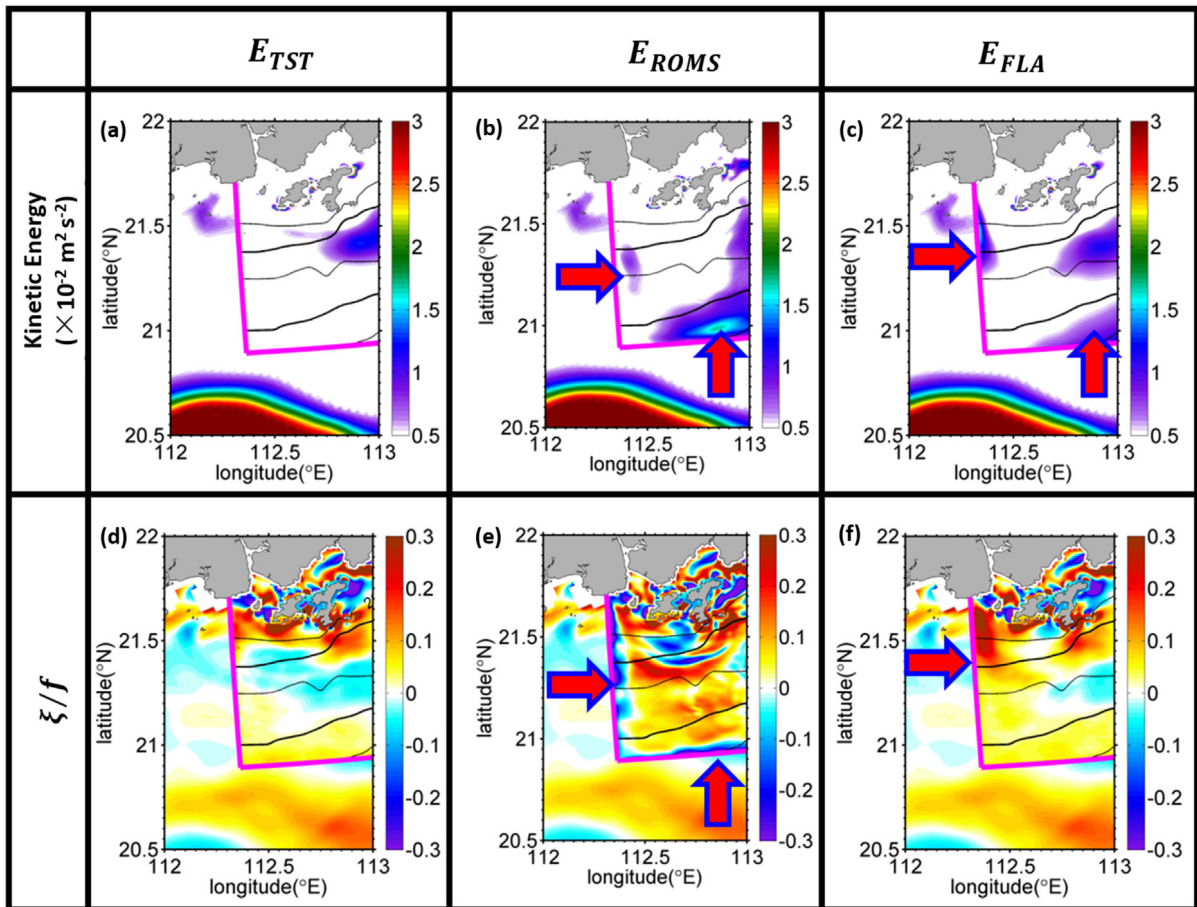


Fig. 9. Like Fig. 8 but zoomed to the western open boundary of the L2 domain. The red arrows in (b, c) and (e, f) highlight the location where the discrepancy between L1 and L2 simulations is discussed.

E_{ROMS} sensitivity experiment. These two new sensitivity experiments are named as E_{FLA} and E_{MAS} . Because the simulations produced using MAS-OBC and FLA-OBC generated similar results (see supplementary information), we selected the E_{FLA} simulation to compare to the results from E_{TST} . The E_{FLA} results are chosen because the physical meanings of the terms in the FLA-OBC algorithm (Eq. (8)) are clearer.

4.1. Transparency of OBCs

Fig. 8 shows the horizontal maps of the depth-averaged (barotropic) kinetic energy and normalized relative vorticity (ξ/f) from E_{TST} , E_{ROMS} , and E_{FLA} . The velocities over the cruise period before computing the kinetic energy and ξ/f are averaged. The results from the

outer domain (P_{TST}) are also presented to illustrate the connection between the two models, and to show the effectiveness of TST-OBC in bridging the two domains. ξ was normalized by f (Coriolis parameter) to represent the Rossby number (R_o). Fig. 9 shows the horizontal maps of kinetic energy and R_o in E_{TST} , E_{ROMS} , and E_{FLA} and reveals more details of the solutions.

The horizontal maps of kinetic energy and R_o show the sensible connection of the barotropic circulation between E_{TST} and P_{TST} and demonstrates the non-reflective spurious kinetic energy along the open boundaries (Figs. 8a and 9a). The eastward shelf current, whose core is over the 30 m isobath (Fig. 5a and b), alternated between positive and negative R_o in the offshore direction at the western boundary (Figs. 8d and 9d). The shelf current near the eastern boundary responded to the eastward branch of the buoyant plume by strengthening (Fig. 8a) with positive R_o over the inshore areas that are shallower than 30 m (Fig. 8d).

When the recommended combination of OBCs in ROMS is used, the connection between E_{ROMS} and P_{TST} produced excessive spurious kinetic energy along the three open boundaries of the L2 domain (Figs. 8b and 9b). These disturbances reflected and grew in the computational domain by creating extensive R_o in E_{ROMS} (Figs. 8e and 9e) to worsen the interior solutions in Fig. 7c and d. This result suggests that, when the recommended combination of OBCs in ROMS are used without adopting the advantages of TST-OBC, the boundary solutions and the interior circulation become contaminated (Mason et al., 2010).

On the other hand, when TST-OBC is used to solve for the baroclinic velocities, temperature, and salinity (Fig. 8c and f) in E_{FLA} , the connections between the L2 and L1 solutions were better defined than in E_{ROMS} . The connections were better defined even when we used FLA-OBC to solve for the barotropic velocities. This finding shows that the L2 simulations improved when an active treatment of the baroclinic velocities, temperature and salinity by TST-OBC is used. However, compared to the solutions from E_{TST} , the results from E_{FLA} still had excessively spurious kinetic energy that accumulated and created discontinuity between E_{FLA} and P_{TST} over the western boundary (Fig. 9c). This energetic distortion caused by FLA-OBC is clear in Fig. 9f where a strong offshore deflection of the shelf current, indicated by a positive R_o , unrealistically occurred. In addition, the connection between E_{FLA} and P_{TST} solutions was distorted over the southern boundary where a notable fake rim current (Mason et al., 2010) was revealed by the heightened spurious kinetic energy (Fig. 8c). Nonetheless, E_{TST} and E_{FLA} performed reasonably well along the up-wave eastern boundary. In the following sections of this paper, results from E_{ROMS} are no longer discussed because it was the worst at connecting the L1 and L2 simulations.

The contrasting baroclinic circulations from E_{TST} and P_{TST} along the western and eastern open boundaries are depicted by their depth-dependent velocities (Figs. 10 and 11). The velocities normal to the western and eastern open boundaries of E_{TST} and E_{FLA} were weaker and less sheared than the velocities in P_{TST} at the down-wave western boundary (Fig. 10a–c). The baroclinic circulations generally agreed with each other at the up-wave eastern boundary (Fig. 11a–c). The solution of E_{FLA} , however, had an unrealistically intensified eastward current in the bottom layer of the western boundary (Fig. 10c). The tangential velocity from E_{FLA} had a very strong offshore rim current over the entire water column (Fig. 10f), but it was absent in P_{TST} and E_{TST} (Fig. 10d and e) along the western boundary of the L2 domain. The unrealistic bottom intensified normal current and rim current indicate that FLA-OBC deflected shelf currents at the down-wave boundary. This finding is consistent with the result revealed by the kinetic energy and R_o in E_{FLA} (Fig. 8c and f). Like the normal velocity, the tangential velocities among these three cases were quite consistent at the up-wave eastern boundary (Fig. 11d–f). The discrepancy between the L2 (E_{TST} and E_{FLA}) and L1 (P_{TST}) domains mainly occurred at the western boundary. In the following sections, the discussion focuses on the effectiveness of the OBCs in producing realistic circulation at the western boundary.

The density differences between E_{TST} and P_{TST} are shown in Fig. 12a, and the density differences between E_{FLA} and P_{TST} are in Fig. 12b. Fig. 12c and d show the corresponding changes in velocities. These velocities normal to the open boundaries are calculated by subtracting the barotropic velocities from the baroclinic velocities in the water column. We averaged the properties shown in Fig. 12 over the cruise period. The density differences ($<1.0 \text{ kg m}^{-3}$) between L1 (P_{TST}) solution and those from E_{TST} and E_{FLA} (Fig. 12a and b) were mainly caused by the strengthened westward propagation of the buoyant plume and weaker upslope invasion of shelf water associated with the upwelling circulation in E_{TST} and E_{FLA} . These differences in the density affected the baroclinic velocities by strengthening the eastward velocity in the buoyant plume and weakening the velocity in the lower layer (Fig. 12c and d). The contribution of the density structure to the baroclinic velocities was weaker in E_{TST} and E_{FLA} than in P_{TST} (not shown), suggesting that when the model resolution increased, the cross-shore density gradient weakened, and the velocity component normal to the boundary diminished because of the thermal-wind dynamics.

It is clear that, due to the adaptation of the active TST-OBC for tracers, which is geostrophically consistent to the velocity fields in E_{TST} and E_{FLA} , the density field over the western boundary simulated the hydrographic structures well (Fig. 12a and b). However, the responses of the baroclinic velocities in E_{TST} and E_{FLA} were different. Although the impacts of the density field on the baroclinic velocities normal to the boundaries were comparable (Fig. 12c and d), the total baroclinic velocities were only sensibly simulated in E_{TST} (Fig. 10b) and were greatly distorted in E_{FLA} (Fig. 10c). This leads us to conclude that the reflective barotropic solutions by FLA-OBC (Fig. 8c and f) transmitted to the baroclinic velocities and undermined the connectivity between the L1 and L2 domains. In E_{FLA} , transmitting excessive disturbances from the barotropic to the baroclinic circulation prevented a westward current from forming in the nearshore region of the western boundary (Fig. 10b).

4.2. Time-dependent OBCs

In this section, the temporal response of kinetic energy and R_o near the open boundaries (10 grid cells from the open boundaries) to time-dependent forcing (Fig. 13) is investigated. The absolute value of R_o ($\frac{|\xi|}{f}$) is used to prevent canceling positive and negative ξ , when computing the time series in Fig. 11c and d.

Fig. 13a and b show that the variations of subtidal kinetic energy were more strongly regulated by the intensity of the wind (Fig. 2c) than by the buoyant discharge (Fig. 2d). The variations of wind and current have a correlation coefficient of 0.72. Kinetic energy increased rapidly in E_{TST} and P_{TST} , when the wind forcing transitioned from upwelling- to downwelling-favorable from July 19 to July 21. The intensified kinetic energy lasted about 10 days until July 30 (Fig. 2c). Although the interior kinetic energy in E_{TST} varied in phase with the kinetic energy in P_{TST} and with comparable intensity (Fig. 13b), there was a larger discrepancy near the western boundary, where the kinetic energy in E_{TST} no longer varied in phase with the kinetic energy from the exterior solution (Fig. 13a). This phase difference due to TST-OBC is clearer in the time series of R_o in Fig. 13c and d. It demonstrates that the dynamics of the computational domain modulated the solutions at the open boundaries, although the regional subtidal forces from P_{TST} determined the solutions at the open boundaries of C_{TST} . Mason et al. (2010) also pointed out that R_o in E_{TST} is generally larger than R_o in P_{TST} , partially because increasing the resolution (E_{TST}) resolves more details of the flow structure.

Fig. 13a further shows that the reflective kinetic energy over the western open boundary of E_{FLA} (Fig. 8c) was mainly from disturbances generated after the abrupt change of wind direction from July 19 to July 21. The fact that the kinetic energy at the western open boundary (Fig. 13a) and from the interior solution (Fig. 13b) of E_{FLA} varied coherently in phase with the kinetic energy from P_{TST} indicates

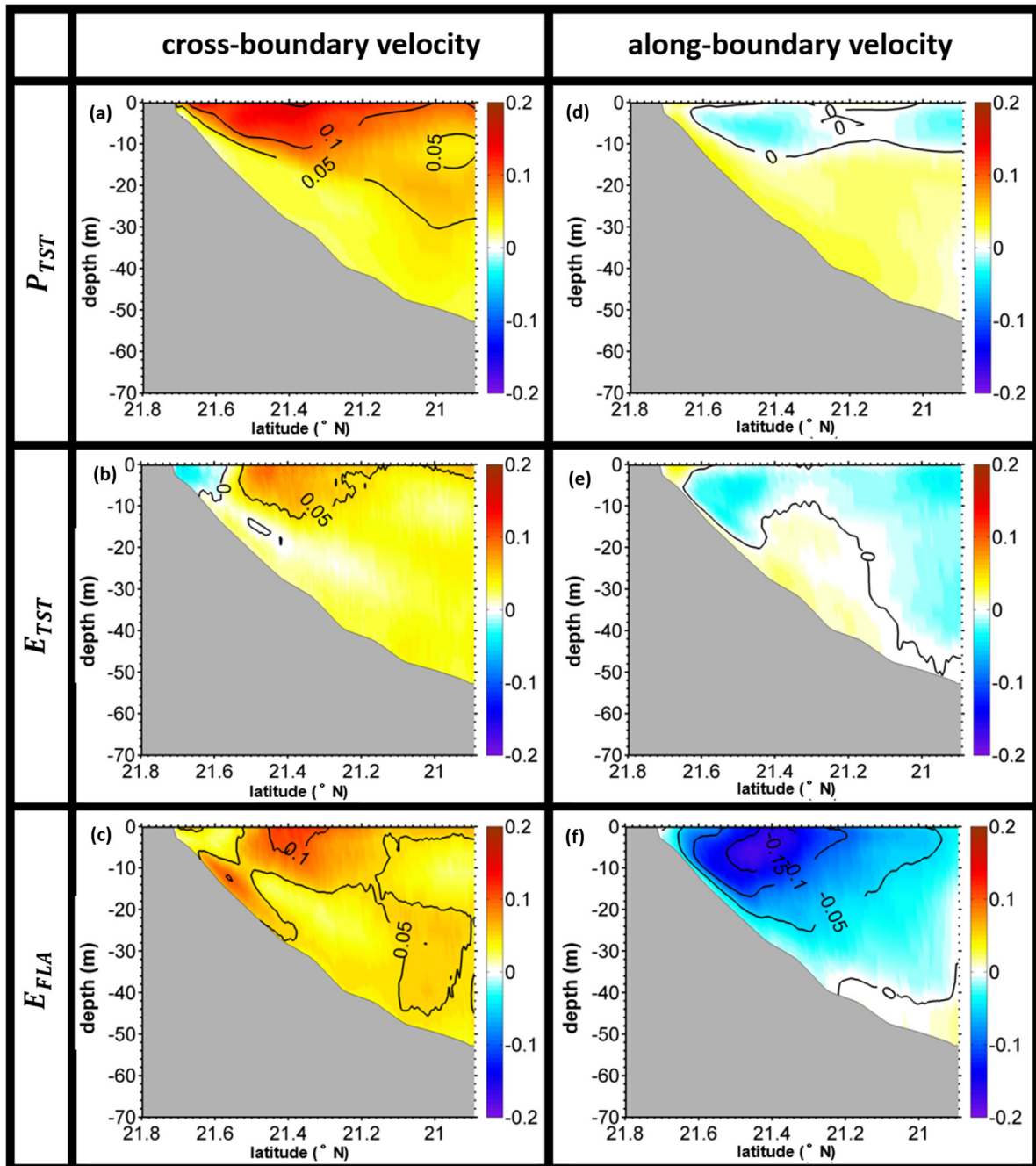


Fig. 10. Cross-shore sections of (a–c) normal and (d–f) tangential velocity components (m s^{-1}) along the western boundary from the (a, d) P_{TST} , (b, e) E_{TST} , and (c, f) E_{FLA} simulations.

that the disturbances generated in the interior were not successfully transmitted by FLA-OBC. This lack of transmission contributed further to the spurious kinetic energy (Fig. 13a) and greatly increased the discontinuity (Fig. 13c) over the shelf neighboring the western boundary of E_{FLA} from July 19 to July 21. The spurious kinetic energy, along with the excessive disturbances, endured for 10 days and undermined the connectivity between the L2 and L1 solutions.

The contrasting performance of TST-OBC and FLA-OBC leads us to conclude that “decomposing” and “active and dual-wave transmitting” for tidally and subtidally generated disturbances in TST-OBC effectively link tidal and subtidal flows in a less-reflective manner than FLA-OBC. Furthermore, TST-OBC has a better response to time-dependent forcing. The “consistent” adaptation of schemes among the barotropic and baroclinic circulations, temperature, and salinity effectively ensures sensible dynamics in the downscaling system. TST-OBC has the advantage of

“tolerating” discrepancy between the E_{TST} and P_{TST} simulations by permitting internally generated disturbances to transmit by imposing phase differences in propagating disturbances between the L2 and L1 solutions.

4.3. Function of the OBC dynamics

In this section, the contribution of each term in Eqs. (6) and (8) to the barotropic velocities normal to the western boundary, are analyzed to determine the functioning mechanism of TST-OBC and FLA-OBC over the western boundary of E_{TST} and E_{FLA} . The time series of total volume transport (Tr) across the western boundary of the L2 domain from our P_{TST} , E_{TST} , and E_{FLA} simulations are shown in Fig. 14a, and the volume transports are defined as $Tr_{(TST)}^P$, $Tr_{(TST)}^E$, and $Tr_{(FLA)}^E$.

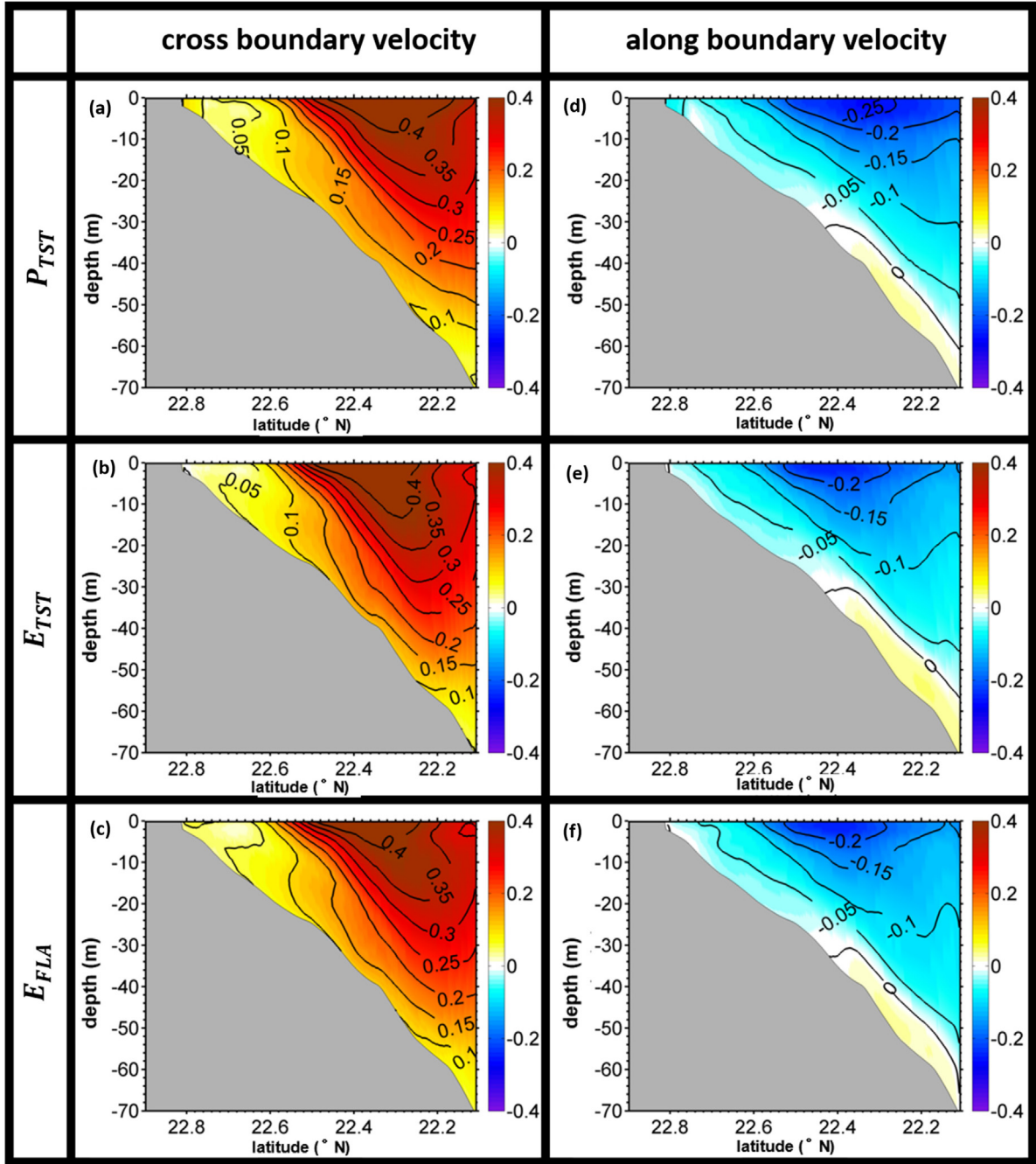


Fig. 11. Cross-shore sections of (a–c) normal and (d–f) tangential velocity components (m s^{-1}) along the eastern boundary from the (a, d) P_{TST} , (b, e) E_{TST} , and (c, f) E_{FLA} simulations.

With Eqs. (6) and (8), these transports are calculated by using the daily averaged \bar{u}_{Rlb}^{n+1} and \bar{u}_b^{n+1} , respectively. Fig. 14b demonstrates the “global” solutions of the “active” TST-OBC and FLA-OBC, which are calculated from:

$$\begin{cases} Tr_{(TST)G}^E = Tr_{(TST)}^E - Tr_{(TST)}^P \\ Tr_{(FLA)G}^E = Tr_{(FLA)}^E - Tr_{(TST)}^P \end{cases} \quad (10)$$

$Tr_{(TST)G}^E$ is determined by three terms: \bar{u}_{Rb}^{n+1} , \bar{u}_{Tlb}^{n+1} and \bar{u}_{Tgb}^{n+1} in Eq. (6) and Table 1. These terms are called $Tr_{(TST)RG}^E$, $Tr_{(TST)TI}^E$ and $Tr_{(TST)TG}^E$, and their time series are shown in Fig. 14c. A similar calculation is performed in E_{FLA} . $Tr_{(FLA)G}^E$ is calculated from \bar{u}_{Tlb}^{n+1} and \bar{u}_{Tgb}^{n+1} in Eq. (8), and the respective transports are called $Tr_{(FLA)TI}^E$ and $Tr_{(FLA)TG}^E$. The time series of these transports are shown in Fig. 14d.

Fig. 14a illustrates that the temporal variation of Tr over the western boundary varied in phase with changes in the wind. $Tr_{(TST)}^E$ and $Tr_{(FLA)}^E$ were weaker than $Tr_{(TST)}^P$ and were modulated by the negative global solutions ($Tr_{(TST)G}^E$ and $Tr_{(FLA)G}^E$) in Fig. 14b to facilitate the link between the L1 and L2 domain. TST-OBC and FLA-OBC transmitted a comparable number of disturbances through $Tr_{(TST)TG}^E$ and $Tr_{(FLA)TG}^E$ (Fig. 14c and d). Although there was a smaller difference in $Tr_{(TST)TG}^E$ and $Tr_{(FLA)TG}^E$, $Tr_{(TST)RG}^E$ varied in phase with $Tr_{(TST)TG}^E$ and the wind (Fig. 14c and d). $Tr_{(TST)RG}^E$ also provided stronger radiation for the disturbances that occurred during or after July 19 to July 21, when the wind abruptly changed from being weakly downwelling-favorable to strongly upwelling-favorable, and when the kinetic energy increased

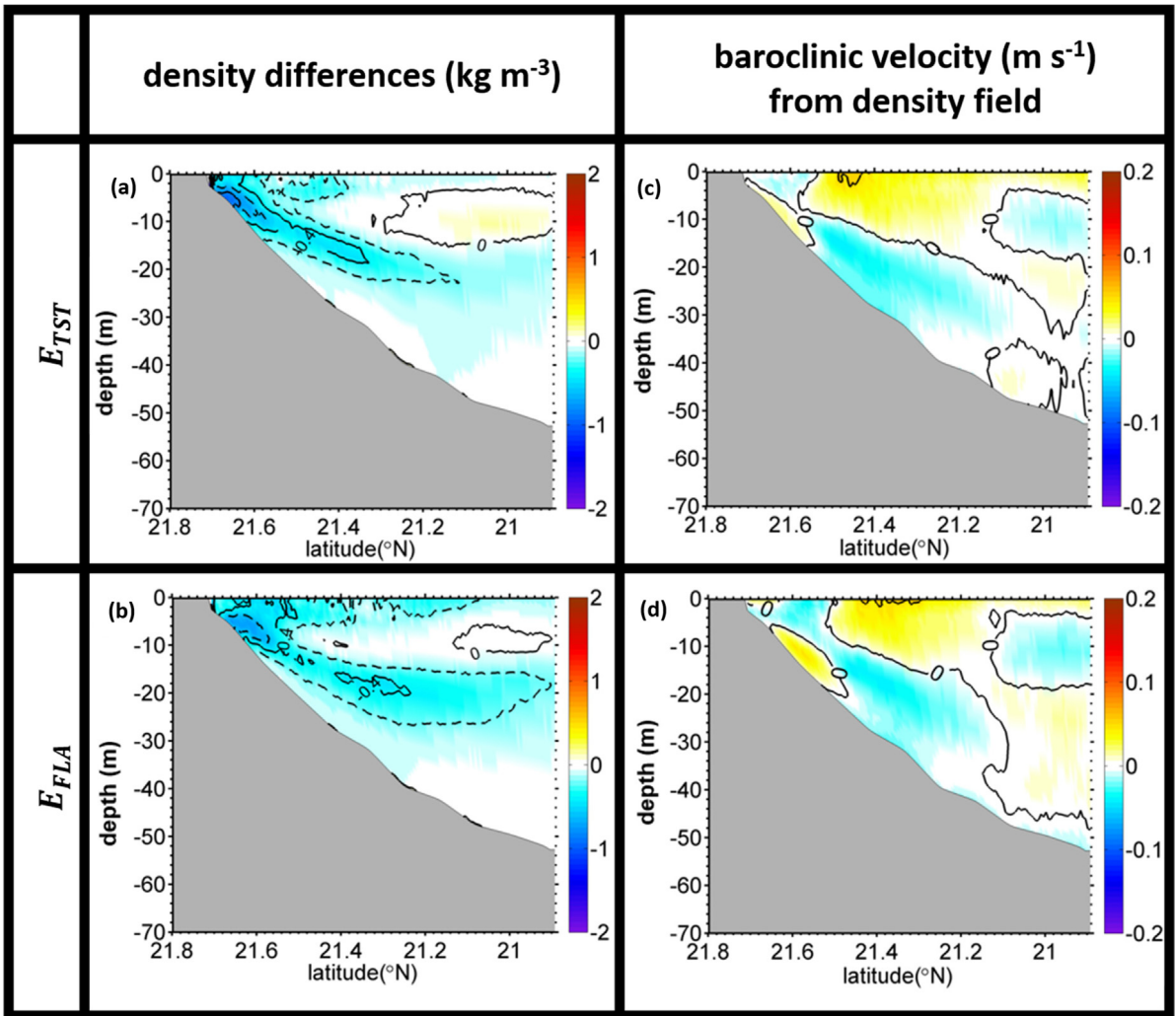


Fig. 12. Density differences (a) between E_{TST} and P_{TST} and (b) between E_{FLA} and P_{TST} . Contribution of the density anomaly to the total baroclinic velocities over the western boundary from (c) E_{TST} and (d) E_{FLA} . The density and velocity fields were averaged over the cruise period.

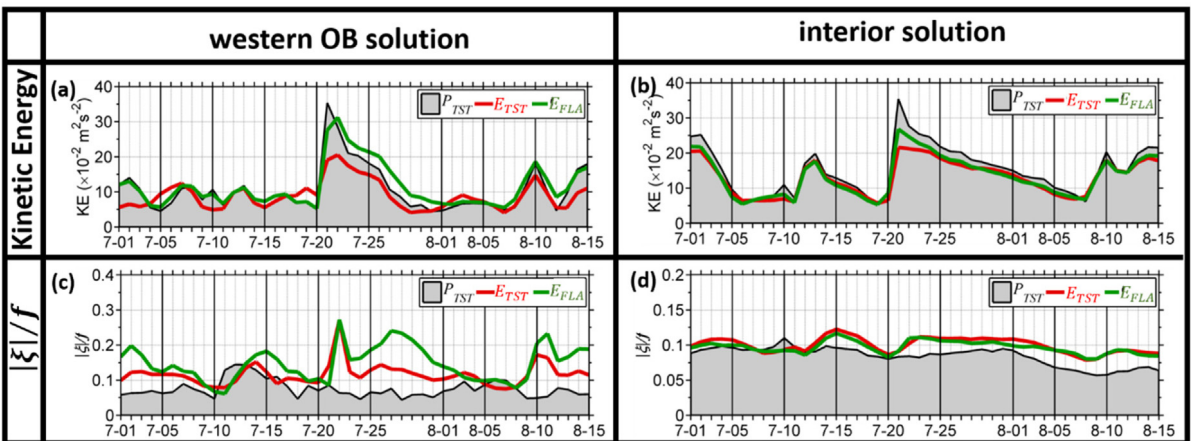


Fig. 13. Time series of simulated (a) kinetic energy and (c) R_o ($\frac{|\xi|}{f}$) from the P_{TST} , E_{TST} , and E_{FLA} neighboring the western boundary of the L2 domain. Time series of simulated (b) kinetic energy and (d) R_o ($\frac{|\xi|}{f}$) from the P_{TST} , E_{TST} , and E_{FLA} averaged over the interior of the L2 domain, excluding the solutions neighboring the open boundaries.

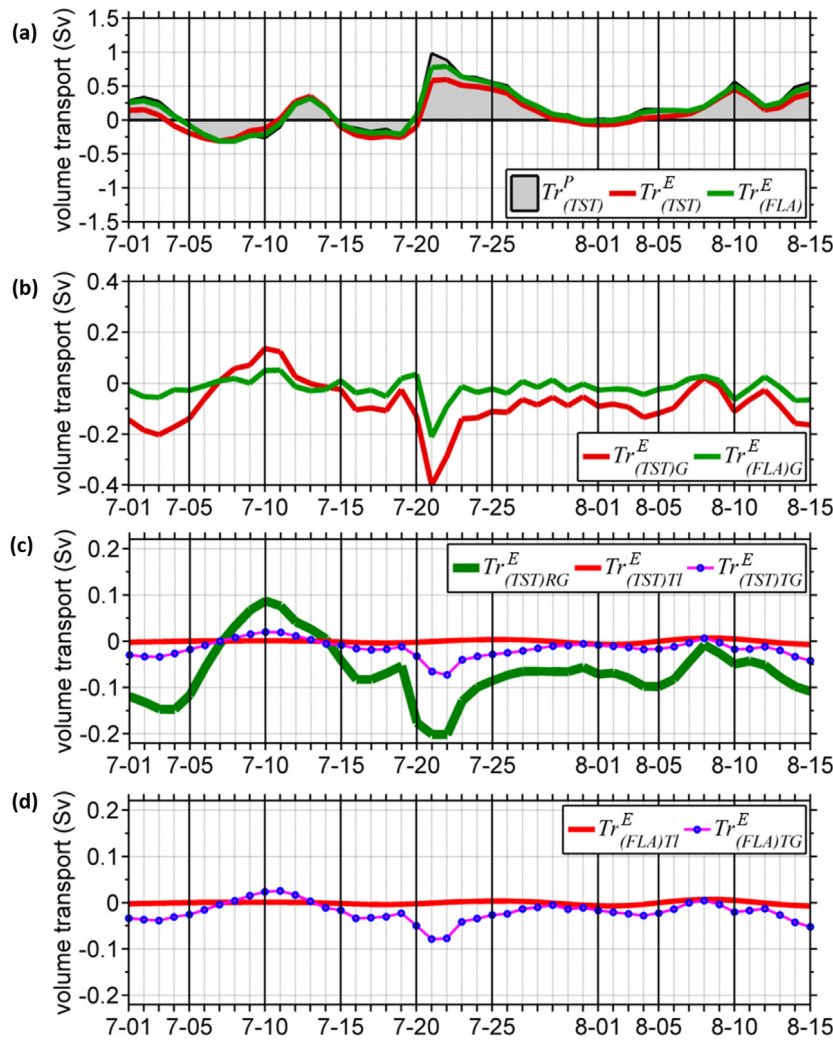


Fig. 14. Time series of simulated (a) volume transport (Sv) across the western boundary of the L2 domain from P_{TST} , E_{TST} , and E_{FLA} ; (b) time series of simulated volume transport (Sv) across the western boundary contributed by $(\bar{u}_b^{n+1} - \bar{u}_{Rib}^{n+1})$ from the global solution for E_{TST} and E_{FLA} ; (c) time series of volume transport (Sv) across the western boundary of the L2 domain from the “global” solution of the subtidal velocity (\bar{u}_{RGb}^{n+1}), tidal velocity (\bar{u}_{Tib}^{n+1}), and the “global” solution from gravity wave propagation (\bar{u}_{TGb}^{n+1}) in Eq. (3) for TST-OBC; and (d) time series of the volume transport (Sv) across the western boundary of the L2 domain from the tidal velocity (\bar{u}_{Tib}^{n+1}) and the global solution from gravity wave propagation (\bar{u}_{TGb}^{n+1}) for FLA-OBC.

extensively over the western boundary (Fig. 13a). The excessive disturbances, illustrated by the barotropic kinetic energy (Fig. 8a), crossed the western boundary (Fig. 14b) with TST-OBC, but were trapped at the western boundary with FLA-OBC.

5. Conclusions

A set of limited-area numerical experiments is conducted to validate the performance of a recently developed “active” TST-OBC for estuarine–shelf circulation jointly driven by spatiotemporally variable wind, buoyancy forcing and tides in the northern South China Sea. TST-OBC is different from the frequently adopted OBC schemes in ROMS because it separates the tidal and subtidal currents by recognizing their distinguishing characteristics, and TST-OBC solves for the tidal and subtidal currents by using “active” schemes. In our experiments, TST-OBC concurrently evacuated the high frequency (tidal component) and low-frequency (subtidal component) disturbances traveling across the open boundaries of the computational domain. TST-OBC performed better than the frequently used schemes in ROMS in downscaling

the concurrent tidal current and subtidal circulation in limited-area simulations from an upscale model with lower resolution.

This study is built based on the work of Liu and Gan (2016) and further examined TST-OBC under variable forcing and over multiple domain nesting applications. While Liu and Gan (2016) validated their experiment under idealized forcing, in our study, a three-level downscaling system with increasing resolution from the South China Sea to the Pearl River Estuary is developed. Tidal forces and subtidal forces with spatial and temporal variability and linked by TST-OBC drove the circulation in our downscaling system. The estuarine–shelf circulation neighboring the Pearl River Estuary where an ultra-high resolution (0.2–1.0 km) is adapted, is focus of this research. The simulations were validated with observations measured during a field cruise from July 1 to August 15, 2015. This research finds found that the strong tidal and subtidal forces jointly drove the circulation inside this computational domain. The subtidal forces included varying wind stress and river discharge that generated a notable buoyant plume enveloped by a sharp density front over the shelf off the Pearl River Estuary.

This research shows that TST-OBC consistently reproduces the tidal elevation and currents. It is also confirmed that TST-OBC simulates

the propagation of the high frequency rapidly propagating tidal waves across the limited-area computational domain. TST-OBC reproduces the variability in the observations with the simulations that show extensive upwelling of shelf waters and bi-directional branching of the buoyant plume in the down-wave and up-wave directions. When Comparing T-S diagrams of simulated and observed temperature and salinity, the correlation coefficient was over 0.95 and the coefficient of determination was over 0.8. The observations and simulations consistently show that the subtidal flow is characterized by the predominant upwelling circulation with synoptic variations in response to wind forcing, especially when the wind reverses direction from weak downwelling-favorable to strong upwelling-favorable.

The effectiveness and functioning mechanism of TST-OBC are investigated by examining the contribution of the terms in the governing equations and referring to results from the frequently used FLA-OBC. We showed that, besides the effectiveness of TST-OBC on the barotropic velocity, the shelf circulation and hydrographic properties in the L2 domain are greatly distorted when the baroclinic velocities, temperature, and salinity are not simultaneously solved by TST-OBC. It is also clear that the improved FLA-OBC by Mason et al. (2010) (MAS-OBC) in the Rutgers ROMS presents results like those from FLA-OBC. With our higher resolution, the transport of shelf current normal to the boundary decreases because of the strengthened westward transport of the buoyant plume and the weakened upslope invasion of deep shelf waters. The decrease in transport in TST-OBC is numerically and physically reproduced by its “*decomposing*” and “*active and dual-waves transmitting*” schemes for the tidal current and subtidal circulation.

FLA-OBC only evacuates disturbances over the open boundaries that are induced by tidal waves. With FLA-OBC, disturbances induced by subtidal flows reside at the open boundaries in barotropic flows. These FLA-OBC disturbances distort the barotropic currents in the along-boundary direction, destroy the hydrodynamics associated with the upwelling circulation, and contaminate the baroclinic component and interior solutions that contribute to the discontinuity between sub-models. This drawback of FLA-OBC is overcome if a “*consistent*” adaptation of TST-OBC in barotropic and baroclinic circulations, temperature, and salinity occurs. When TST-OBC for all parameters is consistently adapted, doing so made the scheme “*tolerate*” discrepancies between the L1 and L2 solutions. The consistent adaptation in TST-OBC numerically and dynamically links the circulation between sub-models in a quasi-seamless manner.

It should be noted that, although TST-OBC is feasible for limited-area numerical applications concurrently driven by extensive and spatiotemporally variable tidal and sub-tidal forces, tidal currents are imposed along the open boundaries by performing tidal prediction. Therefore, harmonic constants for tidal elevation and currents are an important prerequisite for using TST-OBC. Moreover, because the subtidal currents are extracted from the daily-averaged velocities from its upscale exterior solution, the adaptation of the TST-OBC scheme is limited to one-way downscaling applications instead of interactive two-way nesting simulations.

Declaration of competing interest

The authors declare that they have no known competing financial interests or personal relationships that could have appeared to influence the work reported in this paper.

Acknowledgments

This work was supported by the Theme-based Research Scheme (T21-602/16-R, OCEAN_HK project) of the Hong Kong Research Grants Council. We thank the insightful suggestions from two anonymous reviewers. We are grateful to the National Supercomputer Center of Tianhe-1 (Tianjin) and Tianhe-2 (Guangzhou). The model data for this study are produced by the community model ROMS (<https://www.myroms.org/>). The data used in the study are found on the web site, <https://ocean.ust.hk/data/>.

Appendix A. Supplementary data

Supplementary material related to this article can be found online at <https://doi.org/10.1016/j.ocemod.2019.101563>.

References

- Blayo, E., Debreu, L., 2005. Revisiting open boundary conditions from the point of view of characteristic variables. *Ocean Model.* 9, 231–252.
- Bourret, A., Devenon, J.L., Chevalier, C., 2005. Investigation on passive open boundary conditions adapted to the conjunction of strong currents, standing tidal wave and high stratification: application to the French Guiana Continental Shelf. *Cont. Shelf Res.* 25, 1353–1373.
- Carter, G.S., Merrifield, M.A., 2007. Open boundary conditions for regional tidal simulations. *Ocean Model.* 18, 194–209.
- Chapman, D.C., 1985. Numerical treatment of cross-shelf open boundaries in a barotropic coastal ocean model. *J. Phys. Oceanogr.* 15, 1060–1075.
- Egbert, G.D., Erofeeva, S.Y., 2002. Efficient inverse modeling of barotropic ocean tides. *J. Atmos. Ocean. Technol.* 19, 183–204.
- Fairall, C.W., Bradley, E.F., Hare, J.E., Grachev, A.A., Edson, J.B., 2003. Bulk parameterization of air–sea fluxes: Updates and verification for the COARE algorithm. *J. Clim.* 16, 571–591.
- Flather, R.A., 1976. A tidal model of the northwest European continental shelf. *Mem. Soc. R. Sci. Liege* 10, 141–164.
- Gan, J., Allen, J.S., 2005. On open boundary conditions for a limited-area coastal model off Oregon. Part 1: Response to idealized wind forcing. *Ocean Model.* 8, 115–133.
- Gan, J., Allen, J.S., Samelson, R.M., 2005. On open boundary conditions for a limited-area coastal model off Oregon. Part 2: response to wind forcing from a regional mesoscale atmospheric model. *Ocean Model.* 8, 155–173.
- Gan, J., Cheung, A., Guo, X., Li, L., 2009a. Intensified upwelling over a widened shelf in the northeastern South China Sea. *J. Geophys. Res. (Oceans)* 114, <http://dx.doi.org/10.1029/2007JC004660>.
- Gan, J., Li, L., Wang, D., Guo, X., 2009b. Interaction of a river plume with coastal upwelling in the northeastern South China Sea. *Cont. Shelf Res.* 29, 728–740.
- Gan, J., Liu, Z., Liang, L., 2016. Numerical modeling of intrinsically and extrinsically forced seasonal circulation in the China Seas: A kinematic study. *J. Geophys. Res. (Oceans)* 121, 4697–4715.
- Gan, J., Wang, J., Liang, L., Li, L., Guo, X., 2015. A modeling study of the formation, maintenance, and relaxation of upwelling circulation on the Northeastern South China Sea shelf. *Deep Sea Res. II* 117, 41–52.
- Liu, Z., Gan, J., 2016. Open boundary conditions for tidally and subtidally forced circulation in a limited-area coastal model using the Regional Ocean Modeling System (ROMS). *J. Geophys. Res. (Oceans)* 121, 6184–6203.
- Liu, Z., Gan, J., Wu, X., 2018. Coupled summer circulation and dynamics between a bay and the adjacent shelf around Hong Kong: observational and modeling studies. *J. Geophys. Res. (Oceans)* <http://dx.doi.org/10.1029/2018JC013830>.
- Marchesiello, P., McWilliams, J.C., Shchepetkin, A.F., 2001. Open boundary conditions for long-term integration of regional oceanic models. *Ocean Model.* 3 (1–2), 1–20.
- Marsaleix, P., Auclair, F., Estournel, C., 2006. Considerations on open boundary conditions for regional and coastal ocean models. *J. Atmos. Ocean. Technol.* 23, 1604–1613.
- Mason, E., Molemaker, J., Shchepetkin, A.F., Colas, F., McWilliams, J.C., Sangrà, P., 2010. Procedures for offline grid nesting in regional ocean models. *Ocean Model.* 35, 1–15.
- Mellor, G.L., Yamada, T., 1982. Development of a turbulence closure model for geophysical fluid problems. *Rev. Geophys.* 20 (851).
- Oddo, P., Pinardi, N., 2008. Lateral open boundary conditions for nested limited area models: a scale selective approach. *Ocean Model.* 20, 134–156.
- Oey, L.-Y., Chen, P., 1992. A model simulation of circulation in the northeast Atlantic shelves and seas. *J. Geophys. Res.* 97 (20087).
- Oliger, J., Sundström, A., 1978. Theoretical and practical aspects of some initial boundary value problems in fluid dynamics. *SIAM J. Appl. Math.* 35, 419–446.
- Orlanski, I., 1976. A simple boundary condition for unbounded hyperbolic flows. *J. Comput. Phys.* 21, 251–269.
- Palma, E.D., Matano, R.P., 1998. On the implementation of passive open boundary conditions for a general circulation model: The barotropic mode. *J. Geophys. Res. (Oceans)* 103, 1319–1341.
- Palma, E.D., Matano, R.P., 2000. On the implementation of open boundary conditions for a general circulation model: The three-dimensional case. *J. Geophys. Res. (Oceans)* 105, 8605–8627.
- Pawlowicz, R., Beardsley, B., Lentz, S., 2002. Classical tidal harmonic analysis including error estimates in MATLAB using T_TIDE. *Comput. Geosci.-Uk* 28, 929–937.
- Reid, R.O., Bodine, B.R., 1968. Numerical model for storm surges in Galveston Bay. *J. Waterw. Harb. Div.* 94, 33–58.
- Roed, L.P., Smedstad, O.M., 1984. Open boundary-conditions for forced waves in a rotating fluid. *Siam J. Sci. Stat. Comp.* 5, 414–426.
- Shchepetkin, A.F., McWilliams, J.C., 2005. The regional oceanic modeling system (ROMS): a split-explicit, free-surface, topography-following-coordinate oceanic model. *Ocean Model.* 9, 347–404.

- Sommerfeld, A., 1949. Partial differential equation in physics. In: Lectures on Theoretical Physics-Pure and Applied Mathematics, Academic Press, New York, 1.
- Song, Y.T., Haidvogel, D.B., 1994. A semi-implicit ocean circulation model using a generalized topography-following coordinate system. *J. Comput. Phys.* 115, 228–244.
- Tsynkov, 1998. Numerical solution of problems on unbounded domains, a review. [http://dx.doi.org/10.1016/s0168-9274\(98\)00025-7](http://dx.doi.org/10.1016/s0168-9274(98)00025-7).
- Zu, T., Gan, J., 2015. A numerical study of coupled estuary–shelf circulation around the Pearl River Estuary during summer: responses to variable winds, tides and river discharge. *Deep Sea Res. II* 117, 53–64.
- Zu, T., Gan, J., Erofeeva, S.Y., 2008. Numerical study of the tide and tidal dynamics in the South China Sea. *Deep Sea Res. I* 55, 137–154.
- Zu, T., Wang, D., Gan, J., Guan, W., 2014. On the role of wind and tide in generating variability of Pearl River plume during summer in a coupled wide estuary and shelf system. *J. Mar. Syst.* 136, 65–79.